

PREPARED FOR SUBMISSION TO JINST

NTH WORKSHOP ON X

WHEN

WHERE

Reconstruction and classification of tau lepton decays at a future $e^- e^+$ Linear Collider

B. Xu,^{a,1} S. Green,^a J. S. Marshall,^a M. A. Thomson^a

^a*Cavendish Laboratory,*

JJ Thomson Avenue, Cambridge, CB3 0HE, UK

E-mail: xu@hep.phy.cam.ac.uk

ABSTRACT: Seven tau lepton decay modes were studied using simulated data, for the proposed Compact Linear Collider. Tau leptonic physics is important. Its branching ratios measurements provide precision tests of the Standard Model. Spin state of a tau lepton can be used to measure the CP properties of the Higgs boson, via the Higgs to a tau pair decay. Correct classification probability of tau lepton decay is a benchmark of detector performance. In this paper, seven decay modes were reconstructed and classified for centre of mass of 100, 200, 500 and 1000 GeV, and for electromagnetic calorimeter (ECal) square cell sizes of 3, 5, 7, 10, 15, and 20 mm. Major challenges for classification include reconstructing multiple nearby photons as separate entities, and correct association of inner detector tracks to energy deposited in calorimeters. Efficient classification of tau decay mode is achieved. Overall tau lepton hadronic decay correct classification probability is over 90% for $\sqrt{s} = 100$ GeV. For $\sqrt{s} = 200$ GeV, the probability decreases from over 90% to 86% for ECal square cell sizes from 3 to 20 mm. For $\sqrt{s} = 500$ and 1000 GeV, the probability degrades significantly, from over 90% to 77%, and from 86% to 75%, respectively, for the same range of the cell sizes.

KEYWORDS: TODO: Only keywords from JINST's keywords list please

ARXIV EPRINT: [1234.56789](https://arxiv.org/abs/1234.56789)

¹Corresponding author.

Contents

| | | |
|----------|---|----------|
| 1 | Introduction | 1 |
| 2 | Simulation and Reconstruction | 2 |
| 3 | Analysis strategy | 3 |
| 4 | Results | 6 |
| 5 | Electromagnetic calorimeter optimisation | 7 |
| A | Variables for multivariate analysis | 9 |

1 Introduction

The tau lepton has been examined extensively in the past. In particular, detailed studies were performed at the Large Electron Positron Collider (LEP)[1]. The properties of tau lepton decay provide precision tests of the Standard Model and models beyond the Standard Model. Such properties include tau decay branching ratios, and total tau hadronic decay width, which depends on the strong coupling constant. The spin state of tau lepton, which can be inferred from kinematic properties of tau decay products, can be used to measure the CP (the product of charge conjugation and parity symmetries) of the Higgs, via $H \rightarrow \tau^- \tau^+$ channel.

Performance of tau decay mode classification provides a benchmark of detector performance. Since the tau lepton has a very short lifetime [2], it decays in the inner detector before reaching the calorimeter. Typical tau decay products are charged particles, and multiple photons from π^0 . Reconstruction of multiple nearby photons requires an excellent electromagnetic calorimeter (ECal) spatial resolution. Separating different charged particle relies on performance of the inner detector tracking system.

The study was done in the context of the CLIC_ILD detector concept [3] with the PandoraPFA software package [4]. The CLIC_ILD detector concept is designed for the Compact Linear Collider (CLIC) [3] based on the ILD detector [5]. A cross section of the CLIC_ILD detector is shown in figure 1. The detector consists of vertex detectors, tracking detectors, electromagnetic calorimeters, hadronic calorimeters (HCal) and muon chambers. Magnetic field is optimised for the particle flow approach (PFA) to calorimetry [6] with high granularity in both longitudinal and transverse direction, providing unprecedented jet energy resolutions.

Particle flow approach to calorimetry aims to reconstruct individual particles. This makes an efficient tau decay mode classification possible. PandoraPFA, [4], a leading pattern recognition software, has demonstrated its ability to exploit information from high granular calorimeters in the context of future linear colliders. Charged particles are reconstructed by projecting tracks from

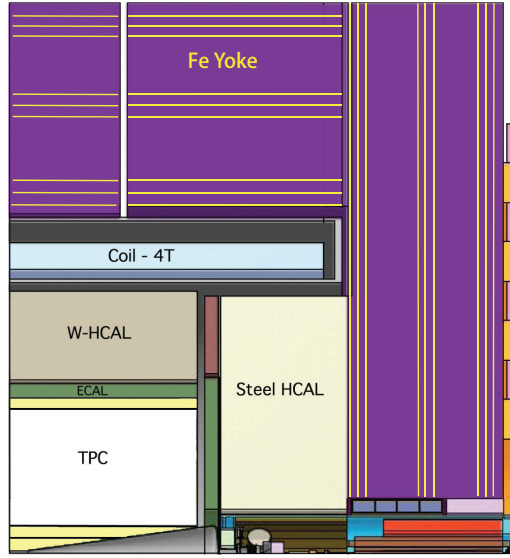


Figure 1: Longitudinal cross section of top quadrant of the CLIC_ILD detector concept, taken from [3]

inner tracking detector and associating calorimeter hits to these tracks. Photons are reconstructed from calorimeter hits in the ECAL, with comparison to expected electromagnetic shower profiles. Neutral hadrons are reconstructed from calorimeter hits in the HCal. The output of the PandoraPFA is Particle Flow Object (PFO), which contains energy, momentum, position, particle id and other information.

Ability to separate tau decay modes relies on photon reconstruction. Calorimeter hits in the ECAL are clustered and carefully isolated from nearby charged particles. These clusters are compared with expected electromagnetic shower profiles, using a likelihood based classifier. Separate algorithms split merged photons and combine small photon fragments to main photons. Photon reconstruction in PandoraPFA is described in [7].

This paper describes the reconstruction and classification of tau lepton decay modes. The classification is used for the ECAL optimisation, with varying ECAL square cell sizes, using different centre of mass energies (\sqrt{s}) for $e^- e^+ \rightarrow \tau^- \tau^+$ interaction.

2 Simulation and Reconstruction

Simulated Monte Carlo (MC) samples were generated with the generator software WHIZARD 1.95 [8], with PYTHIA 6.4 [9] used for the hadronisation and tuned to the LEP results [1]. TAUOLA [10] is used to describe the τ lepton decays with correct spin correlation between decay products. The initial state radiation (ISR) and the beam induced background were not simulated, but final state radiation (FSR) was simulated. This study is aimed for detector optimisation. Hence a clean detector environment is preferred to maximise the effect of the calorimeter design on the performance of the tau decay classification.

Around two millions $e^- e^+ \rightarrow \tau^- \tau^+$ MC simulated events were generated, for each ECal square cell size of 3, 5, 7, 10, 15 and 20 mm, and for each \sqrt{s} energy of 100, 200, 500 and 1000 GeV. In total, 48 millions simulated events were generated. Generated events were considered in the subsequent analysis if they pass a series of generator level selection cuts designed to isolate the effect of the calorimeter design on the performance of the tau decay classification. Around 60% of generated events passed the selection cuts.

Events are discarded if simulated photons convert before reaching the calorimeters. Converted photons would not be reconstructed as photons, and events with converted photons would decrease the classification efficiency. That degradation would not be due to the calorimeter design.

Events are also discarded if total energy of the tau lepton visible decay products is less than 5 GeV. This ensures the decay products properly reconstructed.

Events are further discarded if tau leptons are not with the barrel and end cap calorimeter regions. The polar angle for the end cap region is defined $17.2^\circ < |\theta_Z| < 34.4^\circ$. The polar angle for the barrel region is defined $45.8^\circ < |\theta_Z| < 90^\circ$. Very forward region of the detector is not simulated due to technical reasons. The particle reconstruction was not optimised for the gap region between the barrel and the end cap region for the CLIC_ILD detector. Therefore by confining to the barrel and the end cap region only, a consistent high particle reconstruction efficiency is ensured.

Events were simulated with software MOKKA [11] with the CLIC_ILD detector geometry description, based on the GEANT 4 package [12]. Reconstruction was done with ilcsoft version v01-17-07 [13] and PandoraPFA version v02-02-00 [4], where the photon reconstruction is described in [7].

3 Analysis strategy

Table 1: Branching fractions of the seven τ^- decays in this study[14]. τ^+ decays similarly to τ^- .

| Decay mode | Branching fraction / % |
|------------------------------------|------------------------|
| $e^- \bar{\nu}_e \nu_\tau$ | 17.83 ± 0.04 |
| $\mu^- \bar{\nu}_\mu \nu_\tau$ | 17.41 ± 0.04 |
| $\pi^- \nu_\tau$ | 10.83 ± 0.06 |
| $\rho(\pi^- \pi^0) \nu_\tau$ | 25.52 ± 0.09 |
| $a_1(\pi^- \pi^0 \pi^0) \nu_\tau$ | 9.30 ± 0.11 |
| $a_1(\pi^- \pi^- \pi^+) \nu_\tau$ | 8.99 ± 0.06 |
| $\pi^- \pi^- \pi^+ \pi^0 \nu_\tau$ | 2.70 ± 0.08 |

The seven tau lepton decay modes were considered, shown in table 1. These decay modes cover 92.58 % of all tau decays. The neglected decay modes each have branching fractions below 1%.

This study focuses on the reconstruction and classification of single tau decay. Therefore, two tau leptons in $e^- e^+ \rightarrow \tau^- \tau^+$ channel are separated using thrust variable. Thrust axis is the best fitted line of all particles' momentum. The sign of the dot product between the thrust axis and the particle' momentum separates particles into one of the two collections. Two collections correspond

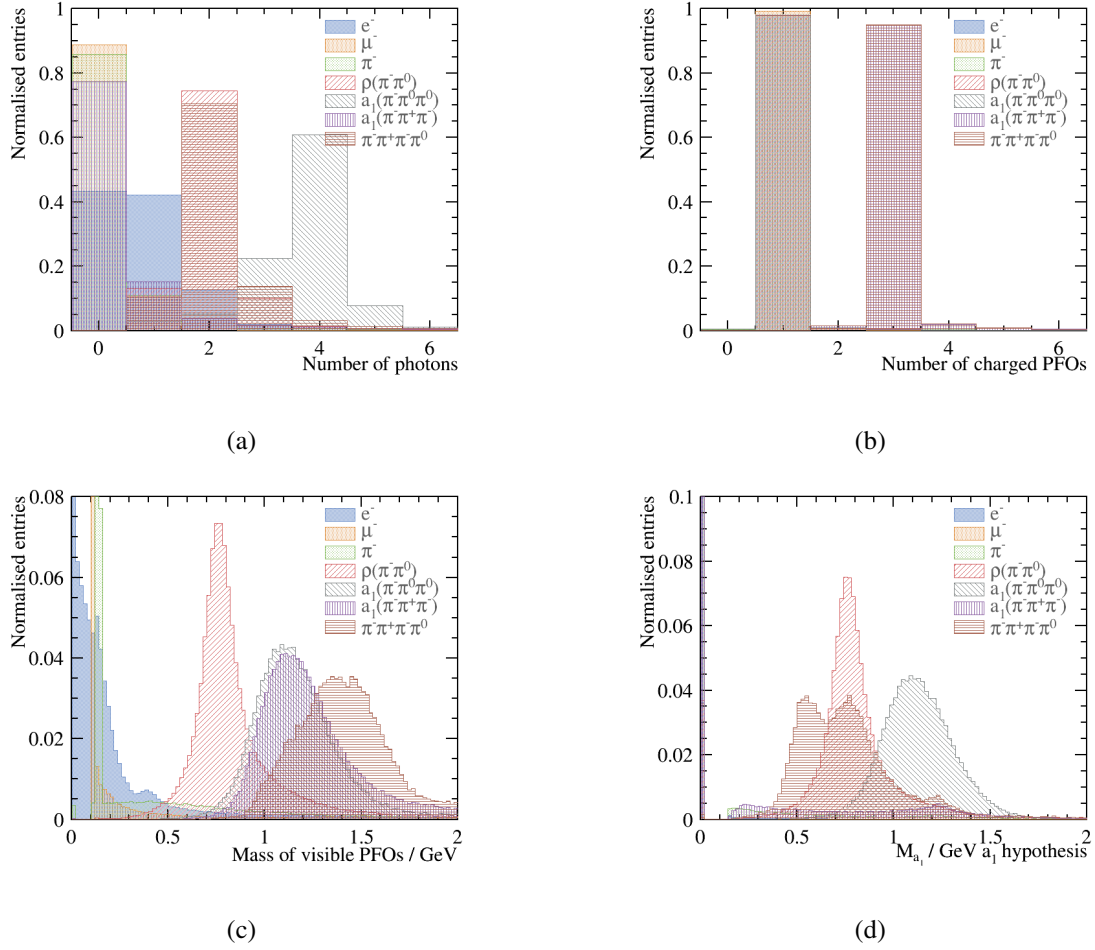


Figure 2: Normalised distribution for discriminative variables for seven tau decay modes, $e^- \bar{\nu}_e \nu_\tau$, $\mu^- \bar{\nu}_\mu \nu_\tau$, $\pi^- \nu_\tau$, $\rho(\pi^- \pi^0) \nu_\tau$, $a_1(\pi^- \pi^0 \pi^0) \nu_\tau$, $a_1(\pi^- \pi^+ \pi^-) \nu_\tau$, and $\pi^- \pi^+ \pi^- \pi^0 \nu_\tau$, with $\sqrt{s} = 100$ GeV for nominal CLIC_ILD detector model. Figure 2a is the number of photons. Figure 2b is the number of charged PFOs. Figure 2c is the invariant mass of visible PFOs. Figure 2d is the invariant mass of $a_1(\pi^- \pi^0 \pi^0)$, calculated with $a_1(\pi^- \pi^0 \pi^0)$ hypothesis.

to decay products of two tau leptons. This method is valid because two taus from $e^- e^+ \rightarrow \tau^- \tau^+$ are largely travelling in opposite direction. Formally the definition of thrust axis is

$$T = \max_{\hat{n}} \frac{\sum_i |p_i \cdot \hat{n}|}{\sum_i |p_i|}, \quad (3.1)$$

where p_i is the particle i 's momentum. \hat{n} is the thrust axis.

A set of discriminative variables were carefully developed, listed in the appendix. The reason for the large number of variables is due to training seven decay modes at once with the multivariate analysis, which will be discussed later. For the ease of discussion and the similarity in event topologies, seven decay modes can be classified into three categories: leptonic decays, one-prong decays with photons and three-prong decays with photons. Leptonic decays refer to $e^- \bar{\nu}_e \nu_\tau$ and

$\mu^- \bar{\nu}_\mu \nu_\tau$. One-prong decays refer to $\pi^- \nu_\tau$, $\rho(\pi^- \pi^0) \nu_\tau$, and $a_1(\pi^- \pi^0 \pi^0) \nu_\tau$. Three-prong decays refer to $a_1(\pi^- \pi^- \pi^+) \nu_\tau$ and $\pi^- \pi^- \pi^+ \pi^0 \nu_\tau$.

The Number of photons is an important variable. It gives an excellent separation, due to excellent photon reconstruction provided by PandoraPFA. As shown in figure 2a, majority of $\mu^- \bar{\nu}_\mu \nu_\tau$, $\pi^- \nu_\tau$ and $a_1(\pi^- \pi^- \pi^+) \nu_\tau$ final states have zero photon reconstructed. Nearly half of $e^- \bar{\nu}_e \nu_\tau$ final state events have one photon reconstructed instead of zero, due to FSR. $\rho(\pi^- \pi^0) \nu_\tau$ and $\pi^- \pi^- \pi^+ \pi^0 \nu_\tau$ have nearly 80% events with two reconstructed photons, whilst $a_1(\pi^- \pi^- \pi^+) \nu_\tau$ have over 60% events with four reconstructed photons. The loss of photon reconstruction efficiency is because the difficulty of separating nearby photons.

The number of charged PFOs, shown in figure 2b, represent number of associate tracks to calorimeter cluters. It can clearly separate the leptonic and 1-prong final states, from the 3-prong final states. The charged PFO selection efficiency of leptonic final states are over 98%.

The invariant mass of the visible PFOs, shown in figure 2c is another powerful variable. $\rho(\pi^- \pi^0) \nu_\tau$, $a_1(\pi^- \pi^0 \pi^0) \nu_\tau$ and $a_1(\pi^- \pi^- \pi^+) \nu_\tau$ distributions show clear resonance at $\rho(770)$ and $a_1(1260)$. $e^- \bar{\nu}_e \nu_\tau$, $\mu^- \bar{\nu}_\mu \nu_\tau$ and $\pi^- \nu_\tau$ distributions show much smaller invariant mass. $\pi^- \pi^- \pi^+ \pi^0 \nu_\tau$ final state has a larger invariant mass than $a_1(1260)$. The $e^- \bar{\nu}_e \nu_\tau$ final state has a long tail of invariant mass due to extra photons from the FSR.

The resonance at $\rho(770)$ and $a_1(1260)$, shown in figure 2c, can be further exploited to enhance the decay modes classification. For example, $a_1(\pi^- \pi^0 \pi^0) \nu_\tau$ decay mode has one π^- and four γ in the final state. By demanding two γ pairs having invariant mass close to that of a π^0 , and invariant mass of one π^- plus four γ close to that of a $a_1(1260)$, resonance at $a_1(1260)$ is enhanced and the loss of efficiency in the reconstruction is compensated. In this example, if fewer than four γ are reconstructed, photon pairs would assume to merged in the reconstruction. This process would demand only one γ pair having invariant mass close to that of a π^0 , and invariant mass of one π^- plus all γ close to that of a $a_1(1260)$. Similarly, if there is fewer than two γ , this process would just demand one π^- plus one γ having invariant mass close to that of a $a_1(1260)$.

Formally, this resonance enhancement procedure is done via a χ^2 minimisation. Using $a_1(\pi^- \pi^0 \pi^0) \nu_\tau$ final state as the exmaple, χ^2 to minimise is defined as

$$\chi_a^2 = \left(\frac{m_{a,fit} - m_a}{\sigma_a} \right)^2 + \left(\frac{m_{\pi^0,fit} - m_{\pi^0}}{\sigma_{\pi^0}} \right)^2 + \left(\frac{m_{\pi^0^*,fit} - m_{\pi^0}}{\sigma_{\pi^0}} \right)^2, \quad (3.2)$$

where $m_{\pi^0,fit}$ and $m_{\pi^0^*,fit}$ are the invariant masses of all possible two photons combinations, σ_a and σ_{π^0} are the half width of the invariant mass distribution of reconstructed a and π^0 using the truth information, and m_a and m_{π^0} are the masses of a and π^0 , taken from [14]. This minisation, resonance enhancement scheme, for $a_1(\pi^- \pi^0 \pi^0) \nu_\tau$ final state is called $a_1(\pi^- \pi^0 \pi^0) \nu_\tau$ hypothesis test, for short.

Figure 2d shows the $m_{a,fit}$ for $a_1(\pi^- \pi^0 \pi^0) \nu_\tau$ hypothesis test. $\rho(\pi^- \pi^0) \nu_\tau$, $a_1(\pi^- \pi^0 \pi^0) \nu_\tau$ and $\pi^- \pi^- \pi^+ \pi^0 \nu_\tau$ final states contribute to the a resonance, although only $a_1(\pi^- \pi^0 \pi^0) \nu_\tau$ final has a real a resonance.

For the $\rho(\pi^-\pi^0)\nu_\tau$ final state, a similar resonance enhancement scheme is used.

Additional variables include number of particles, energies, invariant mass of μ^\pm , e^\pm , γ and charged PFOs. Further separation between $e^-\bar{\nu}_e\nu_\tau$ and $\pi^-\nu_\tau$ decay states are improved with calorimeter information. The information includes comparison of observed and expected electromagnetic shower profile, the matching between inner detector tracks and calorimeter clusters, and the fraction of calorimeter hits registered as minimum ionised particles.

For the multivariate analysis, the multiclass of the TMVA package [15] was used to perform a multiclass classification, which trains the seven final states simultaneously. The multiclass class is an extension of the standard two-class signal-background classifier. For each final state, the multiclass classifier will train the final state as the signal against all other final states as the background. This process is repeated for each final state. The classifier output for a single event is a normalised response for each final state, where the sum is one. The response of each final state of an event can be treated as the likelihood. The event is classified into a particular final state if the final state has the highest classifier output response. The advantage of using the multiclass is that the correlation between different final states are accounted for and the classifier output are correctly adjusted for multiple final states, hence one event can only be classified into one final state. The issue with the multiclass is that discriminative variables for each final state need enter the training stage, resulting in a large number of variables.

Half of the events, randomly selected, were used in the training process and the other half were used for testing. The TMVA multiclass classifier is a boosted decision tree with gradient boosting (BDTG), as it was found to give for the best performance. The MVA classifier is trained and optimised to give the best overall separation across all final states.

4 Results

Table 2: Classification probability for tau decay modes in columns in percentage of $\sqrt{s} = 100$ GeV in the nominal CLIC_ILD detector model. Bold numbers show the correctly reconstructed terms. Numbers less than 0.25% are not shown. Statistical uncertainties are less than 0.25%. ν_τ in final states are not shown.

| Reco \downarrow True \rightarrow | $e^-\bar{\nu}_e$ | $\mu^-\bar{\nu}_\mu$ | π^- | $\rho(\pi^-\pi^0)$ | $a_1(\pi^-\pi^0\pi^0)$ | $a_1(\pi^-\pi^-\pi^+)$ | $\pi^-\pi^-\pi^+\pi^0$ |
|--------------------------------------|------------------|----------------------|-------------|--------------------|------------------------|------------------------|------------------------|
| $e^-\bar{\nu}_e$ | 99.8 | - | 0.9 | 1.1 | 0.8 | - | - |
| $\mu^-\bar{\nu}_\mu$ | - | 99.5 | 0.5 | - | - | - | - |
| π^- | - | 0.3 | 93.2 | 0.9 | - | 0.4 | - |
| $\rho(\pi^-\pi^0)$ | - | - | 4.1 | 93.0 | 10.5 | 0.6 | 2.8 |
| $a_1(\pi^-\pi^0\pi^0)$ | - | - | - | 4.3 | 88.2 | - | 1.0 |
| $a_1(\pi^-\pi^-\pi^+)$ | - | - | 1.0 | 0.3 | - | 96.6 | 6.9 |
| $\pi^-\pi^-\pi^+\pi^0$ | - | - | - | 0.4 | 0.4 | 2.4 | 89.3 |

Table 2 shows classification probabilities for seven tau decay final states of 100 GeV in the nominal CLIC_ILD detector model. An ideal reconstruction would have diagonal terms in the table.

The $\mu^- \bar{\nu}_\mu$ final state has very clear topology, as muon deposits energy in the muon chamber. Therefore, there is little confusion with other final states.

$e^- \bar{\nu}_e$ final state is well separated, due to variables aimed to differentiate early hadronic shower to electromagnetic shower.

For the leptonic decays, the correct classification probabilities are above 99.5%, aided by the tracking system, which offers precision position and momentum measurements

For one prong final states, π^- , $\rho(\pi^-\pi^0)$, and $a_1(\pi^-\pi^0\pi^0)$, the confusion is mainly due to the inability to separate two nearby photons originated from π^0 , which is limited by the calorimeter spatial resolution..

Similarly the confusion between 3-prong final state, $a_1(\pi^-\pi^-\pi^+)$, and $\pi^-\pi^-\pi^+\pi^0$ is caused by same inability to resolve two nearby photons.

Overall a rather high correct classification probability for each tau decay mode is achieved.

5 Electromagnetic calorimeter optimisation

The classification was with $\sqrt{s} = 100, 200, 500, 1000$ GeV. The ECal square cell sizes were varied at 3, 5, 7, 10, 15 and 20 mm, whilst keeping other ECal dimension constant.

The impact of the ECal cell sizes and the \sqrt{s} energies on the classification probabilities of tau decay modes are shown in figure 3. The correct classification probabilities of leptonic decays are not shown, as they are similar across different ECal cell sizes. This is because the e^\pm and μ^\pm identifications mostly rely on the inner detector tracking system, which does not vary in this study. The energy deposited in the calorimeter are used for the association to the inner detector tracks, but it has a small impact on the lepton identification.

Overall, the correct classification probabilities of hadronic decays decrease as the \sqrt{s} energy increases. Taus are boosted at higher \sqrt{s} , the separation between decay products is smaller. Hence it is more difficult to reconstruct multi-particle final states correctly.

The correct classification probabilities decrease as the ECal square cell size increases. Larger cell sizes means that the ECal offers a lower spatial resolutions, making the separation of nearby particles more difficult.

For the $\rho(\pi^-\pi^0)\nu_\tau$ final state, the correct classification probabilities for $\sqrt{s} = 500$ GeV rises for ECal square cell sizes from 15 to 20 mm, and for $\sqrt{s} = 1000$ GeV from 7, to 20 mm. This is compensated with the sharp drop in correct classification probabilities for the $a_1(\pi^-\pi^0\pi^0)\nu_\tau$ final state in the same \sqrt{s} and the same energy. When reconstruction fails to separate nearby photons, the event topologies of two final states are very similar.

For $\sqrt{s} = 100$ and 200 GeV, the correct classification probabilities for the 5 mm ECal cell size is better than that of the 3 mm. One possible explanation is that the PandoraPFA have been optimised for the nominal ILD detector with the 5 mm ECal cell size, which shares the same ECal structure with the nominal CLIC_ILD detector.

Overall classification performance across all decay modes can be compared by constructing a single parameter function, which is a weighted average of correct classification probability for each decay modes. This single parameter allows the direct comparison between different ECal cell sizes, for different \sqrt{s} . It represents an overall classification performance, which MVA is optimised to.

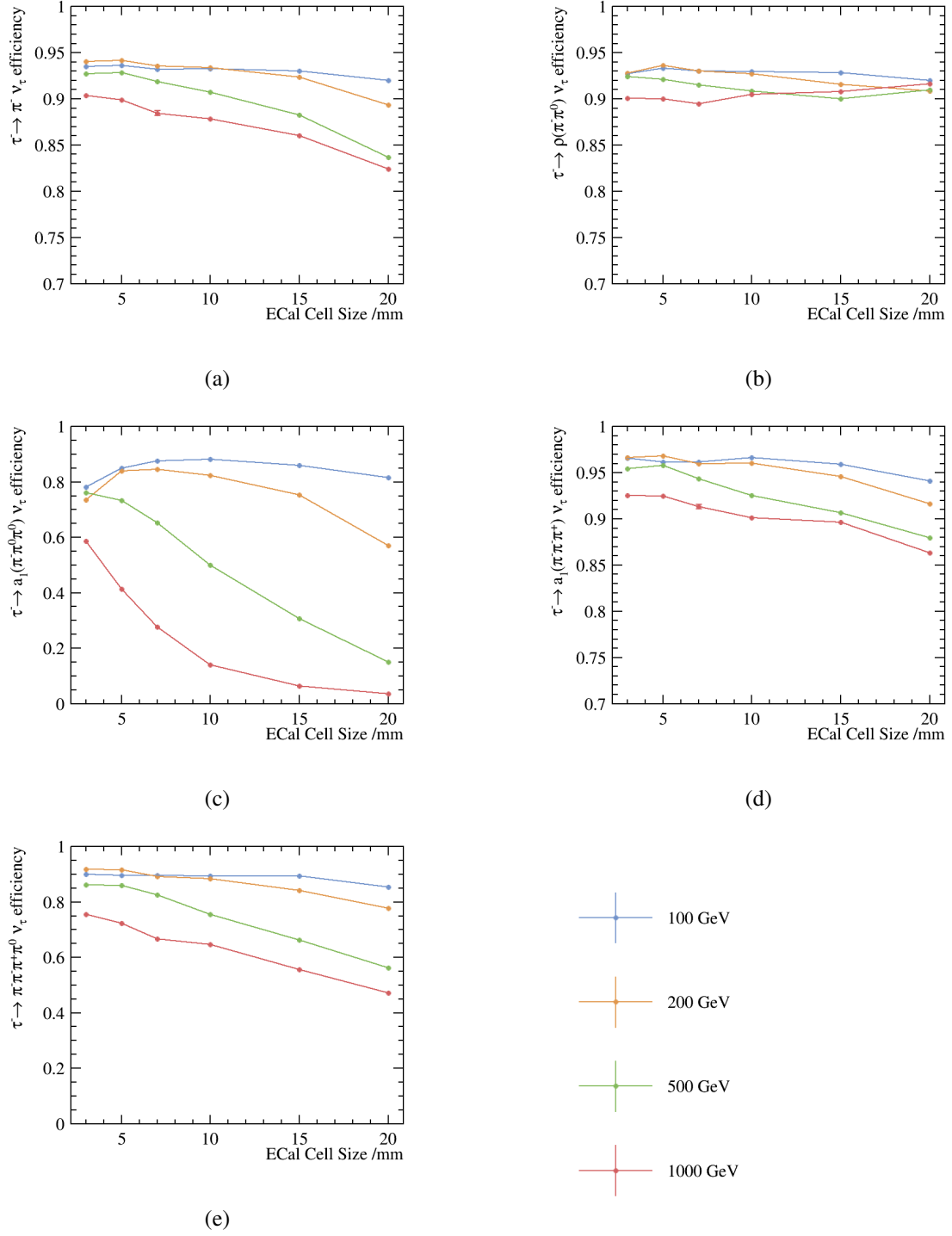


Figure 3: The correct classification probabilities for various final states against the ECal cell size of different c.o.m. energies in the nominal CLIC_ILD detector model. Figure 3a, 3b, 3c, 3d are for the $\pi^- \nu_\tau$, $\rho(\pi^-\pi^0) \nu_\tau$, $a_1(\pi^-\pi^0\pi^0) \nu_\tau$, $a_1(\pi^-\pi^-\pi^+) \nu_\tau$ and $\pi^-\pi^+\pi^0 \nu_\tau$ final states, respectively. Blue, orange, green and red lines are representing $\sqrt{s} = 100, 200, 500$ and 1000 GeV respectively. Note that the y axis are not all the same, for display purposes.

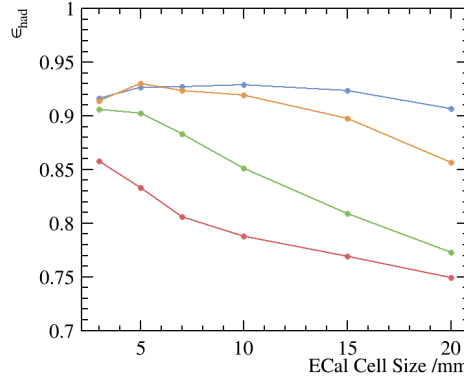


Figure 4: The tau lepton hadronic decay correct classification probability as a function of the ECal square cell size for different \sqrt{s} , in the nominal CLIC_ILD detector model. Blue, orange, green and red lines represent $\sqrt{s} = 100, 200, 500$ and 1000 GeV, respectively.

Formally, the chosen single parameter function is the tau lepton hadronic decay correct classification probability, ϵ_{had} , which is defined as

$$\epsilon_{had} = \frac{(\sum_i Br_i \epsilon_i)}{\sum_i Br_i}, \quad (5.1)$$

where Br_i is the branching ratio of a hadronic decay mode after the generator level cut in section 2. ϵ_i is the correct classification probability for decay mode i . Summation is over five hadronic decay modes. Leptonic decays, $e^- \bar{\nu}_e \nu_\tau$ and $\mu^- \bar{\nu}_\mu \nu_\tau$, were not included because the variations in the leptonic decay correct classification probabilities are small.

Figure 4 shows the tau lepton hadronic decay correct classification probability, ϵ_{had} , as a function of the ECal square cell size for different \sqrt{s} in the nominal CLIC_ILD detector model. ϵ_{had} decreases when ECal square cell sizes increases, and when \sqrt{s} increases.

For $\sqrt{s} = 100$ and 200 GeV, ϵ_{had} for the 5 mm ECal square cell size is better than that of the 3 mm. This is possibly due the optimisation of the software for the nominal ILD 5 mm square cell size.

ECal square cell size has a bigger impact on higher \sqrt{s} . For $\sqrt{s} = 100$ GeV, ϵ_{had} is above 90%. For $\sqrt{s} = 200$ GeV, ϵ_{had} decreases from over 90% to 86% for ECal square cell sizes from 3 to 20 mm. For $\sqrt{s} = 500$ and 1000 GeV, ϵ_{had} degrades significantly, from over 90% to 77%, and from 86% to 75%, respectively, for the same range of the cell sizes.

A Variables for multivariate analysis

Here is a full list of all variables used in the multivariate analysis. Energy of the τ is assume to be the same as the energy of e^\pm beam, which is half of the \sqrt{s} energy. Recoil momenta were calculated assuming the $e^- e^+$ collision happened at the centre of mass energy.

- $\frac{E_{ECal, HCal}}{E_{tot}}$, charged: Sum of energy deposited in ECal and HCal, divided by the energy of charged PFOs

- $\frac{E_{ECal,HCal}}{E_{tot}}$, all: Sum of energy deposited in ECal and HCal, divided by the energy of all PFOs
- m_{vis} : Invariant mass of visible particles in GeV
- $\frac{E_{vis}}{E_{\tau^-}}$: Sum of energy of all PFOs, divided by the energy of τ^-
- $\frac{E_{charged}}{E_{\tau^-}}$: Sum of energy of charged PFOs, divided by the energy of τ^-
- $\frac{E_{\mu^-}}{E_{\tau^-}}$: Sum of energy of muons, divided by the energy of τ^-
- $\frac{E_e}{E_{\tau^-}}$: Sum of energy of electrons, divided by the energy of τ^-
- $\frac{E_{\gamma}}{E_{\tau^-}}$: Sum of energy of photons, divided by the energy of τ^-
- $\frac{E_{\pi^-}}{E_{\tau^-}}$: Sum of energy of charged pions, divided by the energy of τ^-
- $N_{charged}$: Number of charged PFOs
- N_{μ^-} : Number of muons
- N_e : Number of electrons
- N_{γ} : Number of photons
- N_{π^-} : Number of charged pions
- m_{γ} : Invariant mass of photons in GeV
- $m_{charged}$: Invariant mass of charged PFOs in GeV
- $m_{neutral}$: Invariant mass of neutral PFOs in GeV
- m_{π^-} : Invariant mass of charged pions in GeV
- $m_{\pi^0, \rho}(\pi^- \pi^0)$ hypothesis: Fitted invariant mass of π^0 for $\rho(\pi^- \pi^0)$ hypothesis test
- $m_{\rho(\pi^- \pi^0), \rho}(\pi^- \pi^0)$ hypothesis: Fitted invariant mass of ρ for $\rho(\pi^- \pi^0)$ hypothesis test
- $m_{\pi^0, 1, a_1}(\pi^- \pi^0 \pi^0)$ hypothesis: First fitted invariant mass of π^0 , for $a_1(\pi^- \pi^0 \pi^0)$ hypothesis test, ordered by closeness to the true π^0 mass
- $m_{\pi^0, 2, a_1}(\pi^- \pi^0 \pi^0)$ hypothesis: Second fitted invariant mass of π^0 , for $a_1(\pi^- \pi^0 \pi^0)$ hypothesis test, ordered by closeness to the true π^0 mass
- $m_{a_1(\pi^- \pi^0 \pi^0), a_1}(\pi^- \pi^0 \pi^0)$ hypothesis: Fitted invariant mass of $a_1(\pi^- \pi^0 \pi^0)$, for $a_1(\pi^- \pi^0 \pi^0)$ hypothesis test

- $\overline{E_{cell}}$: Average energy deposited in a calorimeter cell in GeV
- $d_{trans,shower}$: Transverse shower width for electromagnetic shower profile, averaged for all clusters in the ECal
- $l_{long,shower}$: Longitudinal start layer for electromagnetic shower profile, averaged for all clusters in the ECal
- $\Delta l_{long,shower}$: Longitudinal discrepancy for electromagnetic shower profile, averaged for all clusters in the ECal
- $\%MIP$: Fraction of calorimeter hits registered as minimum ionised particles, averaged for all clusters in the ECal
- $\frac{E}{p}$: Energy divided by momentum, averaged for all clusters in the ECal

Acknowledgments

The authors would like to thank P. G. Roloff for helping to generate the simulated samples.

References

- [1] ALEPH, S. Schael *et al.*, Phys. Rept. **421**, 191 (2005), hep-ex/0506072.
- [2] DELPHI, P. Abreu *et al.*, Phys. Lett. **B267**, 422 (1991).
- [3] L. Linssen, A. Miyamoto, M. Stanitzki, and H. Weerts, (2012), 1202.5940.
- [4] J. S. Marshall and M. A. Thomson, Eur. Phys. J. **C75**, 439 (2015), 1506.05348.
- [5] ILD Concept Group - Linear Collider Collaboration, T. Abe *et al.*, (2010), 1006.3396.
- [6] M. Thomson, Nucl.Instrum.Meth. **A611**, 25 (2009), 0907.3577.
- [7] B. Xu, Improvement of photon reconstruction in PandoraPFA, in *Proceedings, International Workshop on Future Linear Colliders (LCWS15): Whistler, B.C., Canada, November 02-06, 2015*, 2016, 1603.00013.
- [8] W. Kilian, T. Ohl, and J. Reuter, European Physical Journal C **71** (2011).
- [9] T. Sjostrand, (1995), hep-ph/9508391.
- [10] S. Jadach, Z. Was, R. Decker, and J. H. Kuhn, Comput. Phys. Commun. **76**, 361 (1993).
- [11] P. Mora de Freitas and H. Videau, p. 623 (2002).
- [12] GEANT4, S. Agostinelli *et al.*, Nucl.Instrum.Meth. **A506**, 250 (2003).
- [13] F. Gaede and J. Engels, EUDET Report (2007).
- [14] Particle Data Group, K. A. Olive *et al.*, Chin. Phys. **C38**, 090001 (2014).
- [15] TMVA Core Developer Team, J. Therhaag, AIP Conf.Proc. **1504**, 1013 (2009).